ADVANCED MATERIALS TECHNOLOGIES
www.advmattechnol.de

Large Biaxial Recovered Strains in Self-Shrinking 3D Shape-Memory Polymer Parts Programmed via Printing with Application to Improve Cell Seeding

*Katy Pieri, Di Liu, Pranav Soman, Teng Zhang, and James H. Henderson**

Trapping of strain in layers deposited during extrusion-based (fused filament fabrication) 3D printing has previously been documented. If fiber-level strain trapping can be understood sufficiently and controlled, 3D shape-memory polymer parts could be simultaneously fabricated and programmed via printing (programming via printing; PvP), thereby achieving precisely controlled 3D-to-3D transformations of complex part geometries. Yet, because previous studies have only examined strain trapping in solid printed parts—such as layers or 3D objects with 100% infill—fundamental aspects of the PvP process and the potential for PvP to be applied to printing of porous 3D parts remain poorly understood. This work examines the extent to which strain can be trapped in individual fibers and in fibers that span negative space and the extent to which infill geometry affects the magnitude and recovery of strain trapped in porous PvP-fabricated 3D parts. Additionally, multiaxial shape change of porous PvP-fabricated 3D parts are for the first time studied, modeled, and applied in a proof-of-concept application. This work demonstrates the feasibility of strain trapping in individual fibers in 1D, 2D, and 3D PvP-fabricated parts and illustrates the potential for PvP to provide new strategies to address unmet needs in biomedical and other fields.

1. Introduction

Biomedical devices made of shape memory polymers (SMPs) have been widely studied, but few have made their way from bench to bedside. As a class of smart functional materials, SMPs can "memorize" a permanent shape during fabrication, be programmed to hold a temporary shape, and then, upon application of a stimulus,[1–3] recover back to their permanent shape. Biomedical devices in which SMPs have been studied include self-tightening sutures, expanding synthetic bone grafts, and active cell culture substrates and scaffolds.[4–12]

Traditionally, shape-memory programming of an SMP part, three-dimensional (3D) printed or otherwise, is an independent processing step that occurs following fabrication of the part. Such post-fabrication programming requires controlled mechanically actuated deformation into the desired programmed temporary shape.[1,3] As a result, programming techniques currently in widespread use generally only produce simple, often uniaxial, strains in the part, which limits shape changes to rudimentary forms of expansion, shrinkage, folding, or twisting.[13–15]

The complex and useful SMP part functions and geometries necessary for many prospective applications, including biomedical applications, will require correspondingly complex strain patterns within the part, such as biaxial, torsional, bending, or shear strains, strain gradients, or other spatially varying strains. These complex strain patterns are generally not feasible with current programming techniques, especially in the case of small or intricate part geometries. In fact, precise programming of complex strains remains beyond the current state of the art in shape-memory programming, and use of even relatively simple alternatives to uniaxial programming of 3D SMP parts, such as biaxial strain programming, has remained extremely limited due to the challenges involved in establishing the apparatuses necessary to perform the required mechanically actuated programming. For example, multiaxial programming of a 3D part requires a mechanism to grip the part and apply the desired distributed strains in multiple axes. As a result, to date only a few studies have successfully demonstrated multiaxial programming of 3D SMP parts, and these studies have been restricted exclusively to compressive programming, achieved using manual (literally finger and thumb) manipulation or specialized crimpers or clamps,[8,16] and so only expansile multiaxial recovery has been demonstrated. The lack of methods for

K. Pieri, P. Soman, J. H. Henderson
BioInspired Syracuse: Institute for Material and Living Systems
Department of Biomedical and Chemical Engineering
Syracuse University
Syracuse, NY 13244, USA
E-mail: jhhender@syr.edu
D. Liu, T. Zhang
BioInspired Syracuse: Institute for Material and Living Systems
Department of Mechanical and Aerospace Engineering
Syracuse University
Syracuse, NY 13244, USA
The ORCID identification number(s) for the author(s) of this article can be found under https://doi.org/10.1002/admt.202201997.

DOI: 10.1002/admt.202201997

precisely programming 3D SMPs to both expand and, particularly, contract in complex ways is a critical hurdle to broader application of SMP parts.

Reports in which strains were found to be induced and trapped during printing of "four-dimensional" (4D) SMP parts[17–19] suggest a means by which current programming limitations could be overcome. 4D printing—the 3D printing of SMPs and other functional material parts—has emerged as a promising method for creating complex and highly tailorable devices.[14] Already, SMPs fabricated by 3D printing and programmed post-fabrication by mechanically actuation have shown great potential for meeting the needs of biomedical applications, where the ability to create intricate, patient-specific geometries is desirable.[20,21] Despite the potential of 4D printing, challenges associated with the traditional post-fabrication programming of 4D printed SMP parts have limited progress and hampered widespread adoption. However, reports of strain-trapping during extrusion-based (fused filament fabrication; FFF) printing[17–19,22] suggest that a localized stretching and shape-memory programming step can be mimicked while the polymer is heated and extruded out of the nozzle of the 3D printer, whereby strain is produced and trapped as the polymer fiber is pulled and cooled (**Figure 1**). Supporting the potential of this effect to be exploited for shape-memory programming, a similar but less spatially controlled effect to program SMP scaffolds during fabrication by electrospinning has previously been shown.[4,10,23]

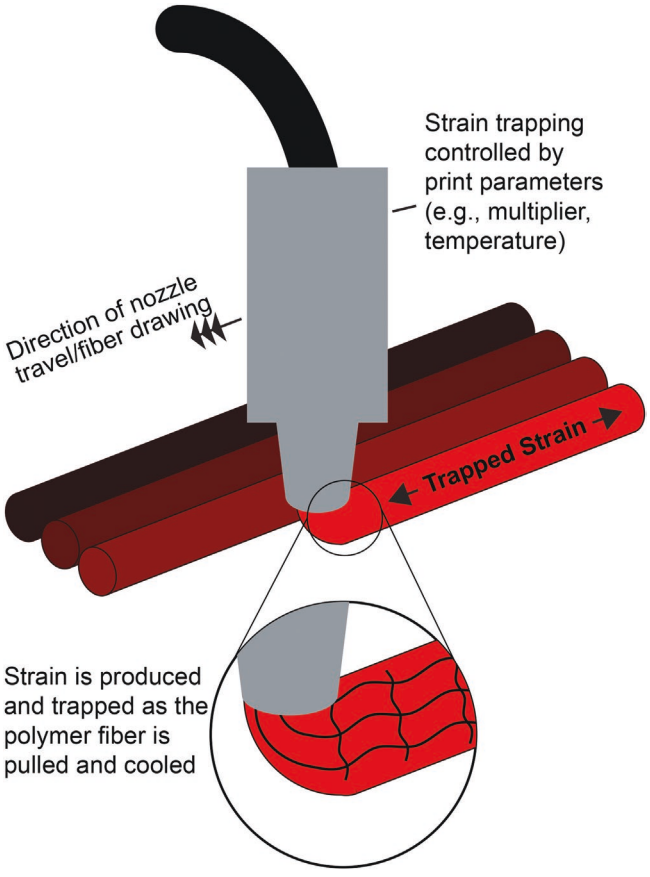

Figure 1. Overview of the fundamental material and mechanical aspects of the Programming via Printing (PvP) approach.

In prior reports of strain-trapping during 3D printing, trapped strains were often considered a flaw in the fabrication process due to potential warped or contracted final parts.[24] As a result, the intentional exploitation of the strain trapping mechanism during printing to direct shape change after printing has been examined by only a few studies, and those studies have only examined strain trapping in solid printed parts, such as layers or 3D objects with 100% infill.[25–27] In particular, Bodaghi et al.[18] designed self-expanding/shrinking actuators, which showed anisotropy in Polyjet printed parts.[28] The same group demonstrated that temperature and printing speed affected the amount of pre-strain in FFF printed 3D beams. Similarly, Hu et al.[19] showed that pre-strain increases with the thickness of the printed parts and observed a Poisson effect upon recovery. While these studies have examined strain trapping in solid components, the extent to which strain can be trapped in individual fibers or in fibers that run across negative space (e.g., voids within porous structures and matrices) has not been studied.

If strains trapped during the 3D printing process can be sufficiently understood and controlled at the fiber level, 3D SMP parts could be simultaneously fabricated and programmed during printing—a process we refer to hereafter as Programming via Printing (PvP)—thereby achieving precisely controlled 3D-to-3D transformations of complex part geometries. Achievement of such single-step fabrication and programming of self-morphing, 3D-to-3D SMP parts could not only lead to a fully automated fabrication process for 4D printed parts[13,29] but also provide a means for programming complex patterns not achievable with current programming paradigms, such as strain gradients or uniform shape change for non-uniform structures. Before PvP can be realized, however, fundamental aspects of the PvP process and the potential for PvP to be applied to printing of porous 3D parts must be better understood.

With the goal of using PvP to achieve single-step fabrication and programming of self-morphing 3D parts and to overcome challenges with multiaxial strain programming and shape change, the fundamental purpose of this work is to study the extent to which strain can be trapped in individual fibers or in fibers that run across negative space and the extent to which infill geometry affects both the magnitude and recovery pattern of trapped strain in porous PvP-fabricated 3D printed parts. Using the understanding achieved, multiaxial shape change of porous PvP-fabricated 3D parts is also for the first time studied, modeled, and applied in a proof-of-concept application. To achieve these goals, SMP single-line (1D) and single-layer (2D) samples are printed while systematically varying temperature, extrusion multiplier (which controls the volumetric flow rate of polymer extrusion relative to nozzle translational velocity), and fiber orientation and the resultant PvP samples characterized by optical imaging and modeled by finite element analysis. Using print parameters identified in the 1D and 2D studies, cubic scaffolds (3D) are printed using two types of infill pattern and the resultant 3D-to-3D contractile shape changing samples similarly characterized and modeled. Lastly, we use the findings to apply PvP to a proof-of-concept application—cell seeding for tissue engineering—to demonstrate the potential for PvP to overcome current programming limitations and address unmet needs in biomedical and other fields.

2. Results and Discussion

2.1. Single Line Samples (1D)

To evaluate FFF printing parameters that contribute to trapped strain and to explore the magnitude of strain that can be trapped into a single fiber, single 1D lines were printed using a shape-memory thermoplastic polyurethane (SMP MM4520, SMP Technologies, Japan) filament at a constant speed (4200 mm min^{-1}) with systematically varied temperature (215 and 225 °C) and extrusion multiplier (0.95 and 1.00). When recovered via immersion in a 70 °C water bath for 5 min, the single line samples curled, transitioning from the original straight lines into arcs and circles, suggesting the presence of a tensile strain gradient through the thickness of the single fibers (**Figure 2**). Temperature had a significant effect on trapped strain ($p = 0.02$; Figure S1, Supporting Information), but multiplier did not for the two values tested ($p = 0.94$). Specifically, samples printed at a lower temperature trapped a higher mean tensile strain (7.3 ± 3.1%) than did those printed at a higher temperature (4.9 ± 2.4%; Figure S1, Supporting Information).

The observed bending could be explained by the cooling of the single fiber, where the midline of the bottom portion (closest to the build plate) of the fiber cools more slowly due to the distance from the air. The material in all other outer surfaces of the fiber allow for faster cooling. Similar bending was observed previously in 3D samples built from solid sheets of fibers and was explained to be due to different trapped strain values resulting from the different conditions that exist at each layer during the printing process.[18,19] For example, lower and middle layers are reheated as the nozzle deposits more molten polymer on top of them. Layers at the top do not get additional heat. Bodaghi et al. take advantage of this process and has used this heating gradient model to predict the final geometry of solid 4D printed parts using input parameters of temperature and printing speed.[22]

Although the present study focused on a single shape-memory thermoplastic polyurethane (SMP MM4520), preliminary experimentation (data not shown) has produced similar strain trapping in individual fibers with both another commercial shape-memory thermoplastic polyurethane (SMP MM3520) from the same vendor and with a shape-memory thermoplastic polyurethane (featuring alternating hard segments of polyhedral oligomeric silsequioxane and biodegradable, amorphous soft segments of polylactide/caprolactone copolymer) originally developed for use as a biodegradable stent coating[30] with we have demonstrated strain trapping during electrospinning.[4,10,23] These finding suggest that the observed effects are likely to be broadly applicable to thermoplastic polyurethanes suitable for FFF printing. In addition, the prior work by Bodaghi and colleagues examining strain trapping in solid components included work that employed polylactic acid,[22,28] suggesting that the observed effects are likely applicable not only to polyurethanes but to diverse FFF printable thermoplastic chemistries. The thermoplastic chemistries studied here and in prior work all appear to trap strains through a similar mechanism, in which strain is produced and trapped as the polymer fiber is pulled and cooled, but further study will be required to understand the relationship between polymer properties and strain trapping during FFF, the extent to which the relationship differs from that governing strain trapping during traditional post-fabrication programming, and the material design principles to be employed to optimize printable thermoplastic materials for maximal control over strain trapping.

2.2. Single Layer Rectangular Samples (2D)

To further evaluate FFF printing parameters that contribute to strain trapping, to explore the magnitude of strain that can be trapped into a single layer of fibers, and to characterize the resulting geometries once the layer is triggered to change shape, single layer 2D rectangles were printed using the same temperatures and multipliers as the single line experiments but additionally printed with varied fiber orientations (0°, 45°, or 90° relative to the long axis).

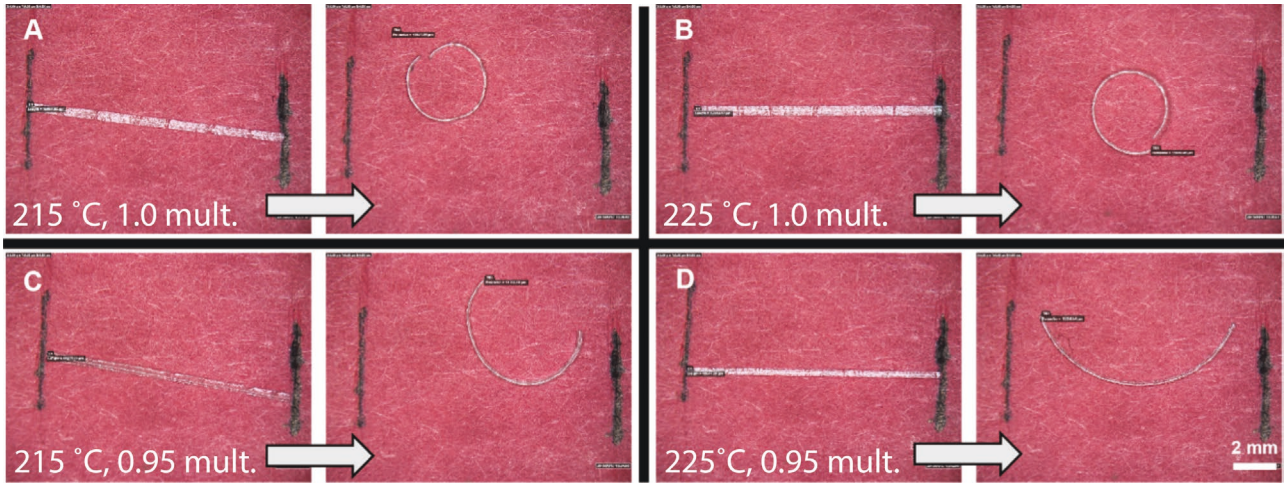

Figure 2. Representative images of single line samples before and after recovery when printed at temperatures of A,C) 215 °C or B,D) 225 °C with an extrusion multiplier of 1.0 (A, B) or 0.95 (C, D). When curling upon recovery, the concave side of all single line (1D) and rectangular (2D; Figure 3) samples was that which had not been in contact with the build plate during printing.

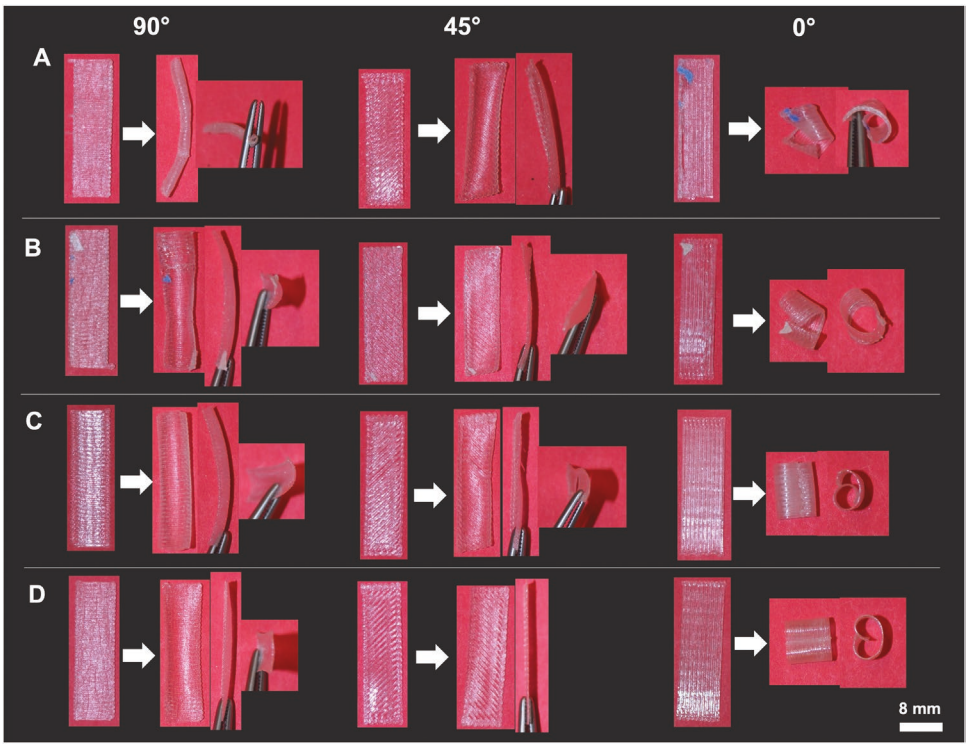

Figure 3. Representative images of 2D rectangular samples before and after recovery when printed with varied fiber orientations (0°, 45°, or 90° relative to the long axis) and printing temperature and multiplier: A) 215 °C, 1.0; B) 225 °C, 1.0; C) 215 °C, 0.95; and D) 225 °C, 0.95.

When recovered at 70 °C using a dynamic mechanical analyzer (DMA), the 90° samples curled along the length of the fibers to form tubes around the sample long axis (**Figure 3**). The 45° samples curled along the length of the fibers to twist the samples into a tube. The 0° samples curled along the length of the fibers to form tubes around the sample short axis. When the 0° samples were used to measure the trapped strain along the length of the fibers, corresponding to the 0° sample long axis, the trapped strain was found to be significantly affected by temperature ($p = 0.0088$), with the lower temperature yielding higher mean strain (27.5 ± 8.7%) than the higher temperature (16.3 ± 7.8%; Figure S2, Supporting Information). Neither the multiplier nor interactions between temperature and multiplier had any significant effect.

2.3. Modeling of Single Line (1D) and Single Layer (2D) Samples

To develop a model fitting of the experimental data and simulate the shape change due to the strains trapped within the samples, we introduced an active deformation to a hyper-elastic model through a multiplicative decomposition of the total deformation gradient tensor. The simulation successfully captured the experimentally observed bending of the 1D single line geometry (**Figure 4**). The bending is likely due to a non-uniform relaxation during printing, which upon cooling causes a gradient of trapped strain. As such, linearly distributed residual strain field along the z direction was adopted (Figure 4B), and an example of a printed single line was simulated with length (L) as 12 mm, thickness (t) as 0.3 mm, and width (w) as 0.3. The residual strain was set to 0.15 at the bottom surface ($z = 0$) and 0.03 at top surface ($z = t$).

The 2D rectangle was simulated with length (L) as 28 mm, width (w) as 8 mm, and thickness (t) as 0.2 mm (**Figure 5**). The printing direction and resulting fiber orientation was set as 45° (Figure 5A). As the value and gradient of residual strain was increased, the rectangle wrapped into a helix (Figure 5B).

2.4. Cubic Scaffolds (3D)

To study the extent to which strain can be trapped in fibers that run across negative space in porous PvP-fabricated 3D printed parts, cubes possessing pores of three different dimensions were printed to observe changes in pore size and in bulk sample size. The fiber orientation was held constant in each layer, so that contraction would occur in only one direction. When recovered via immersion in a 70 °C water bath for 10 min, the cubes contracted in the direction of printing and the dimensions changed from 16 × 15 × 16 mm to 16 × 12 × 18 mm (**Figure 6**). The total area of the top of the cube decreased by 20%. Large pores contracted by 67.0 ± 2.9% of their original area, while the medium and small pores contracted 55.3 ± 18.3% and 51.9 ± 8.2%, respectively.

2.5. Modeling of Cubic Scaffolds (3D)

Finite element analysis was conducted to understand the active shape change of a cube with a porous lattice where fiber

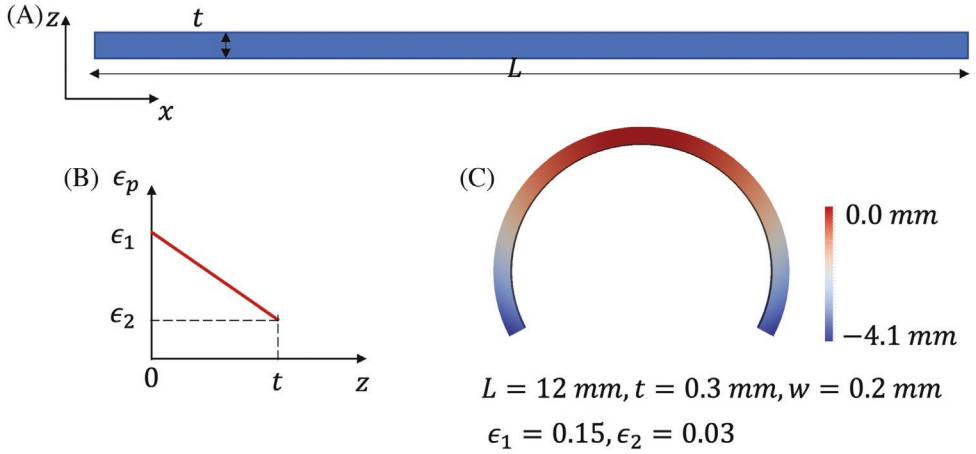

Figure 4. A) The schematic of a 1D printed fiber. B) Gradient of the residual strain along the *z* direction (normal to the printing plane). C) A representative example of curved fiber after triggering (w is the width of the fiber). The color scale indicates the displacement of *z* direction.

orientation was in a uniform direction (along *x* axis; Figure S3, Supporting Information). Upon triggering there is contraction in the *x* direction and expansion in the *z* direction, while the *y* direction remains unchanged, consistent with the behavior of the porous cube geometry (Figure 6).

2.6. Linear and Hexagonal Infill Geometry

To study the extent to which infill geometry affects both the magnitude and recovery pattern of trapped strain in porous PvP-fabricated 3D printed parts, cubes measuring 9.5 × 9.5 × 9.5 mm were designed using CAD (Autodesk Inventor) and printed at 65% infill with either a linear pattern (alternating between 0° and 90° per layer to create pores) or a hexagonal pattern.

Upon recovery, the linear-infilled cube contracted non-uniformly in both fiber directions for a 35.4% change in total area (**Figure 7**). Fibers along the x direction contracted by 28.5 ± 1.1%, while fibers in the y direction contracted by 17.0 ± 0.8%. The area of the pores decreased 49.9 ± 3.2%. The hexagonal-infilled cube contracted uniformly for a 34.8% change in total area. Fibers contracted by 27.3 ± 2.1%. The area of the pores decreased 80.6 ± 6.3%.

Differences in fiber-to-fiber fusion (welding) during printing may be responsible for some observed effects. In cubes with linear infill alternating between 0° and 90° per layer, we saw a 35.4% change in area, however the contractions in the 0° (*x*) and 90° (*y*) directions were not uniform. This suggests that the fusion points where each fiber connects to its orthogonal neighbor acts as anchors and impede strain release, potentially due to a competing Poisson effect. Cubes with hexagon infill

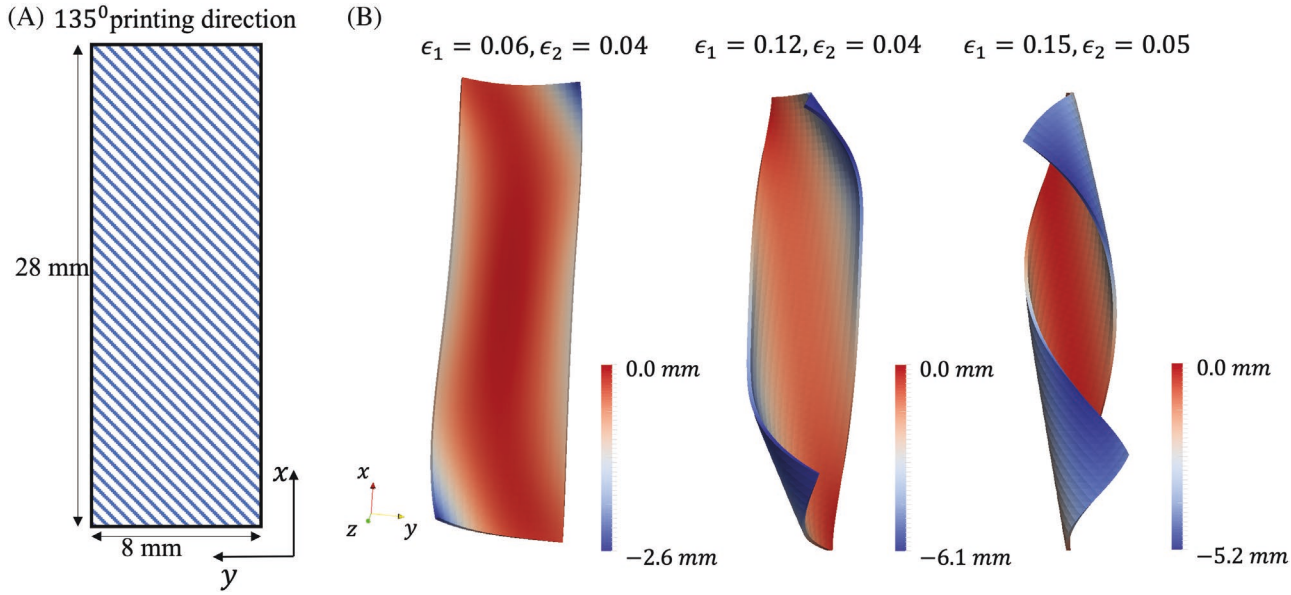

Figure 5. A) The schematic of a 2D printed rectangular sample with the fiber orientation as 45° and thickness (*t*) as 0.2 mm. B) Deformed configurations of the sample at different levels of residual strain. The color scale indicates the displacement of *z* direction.

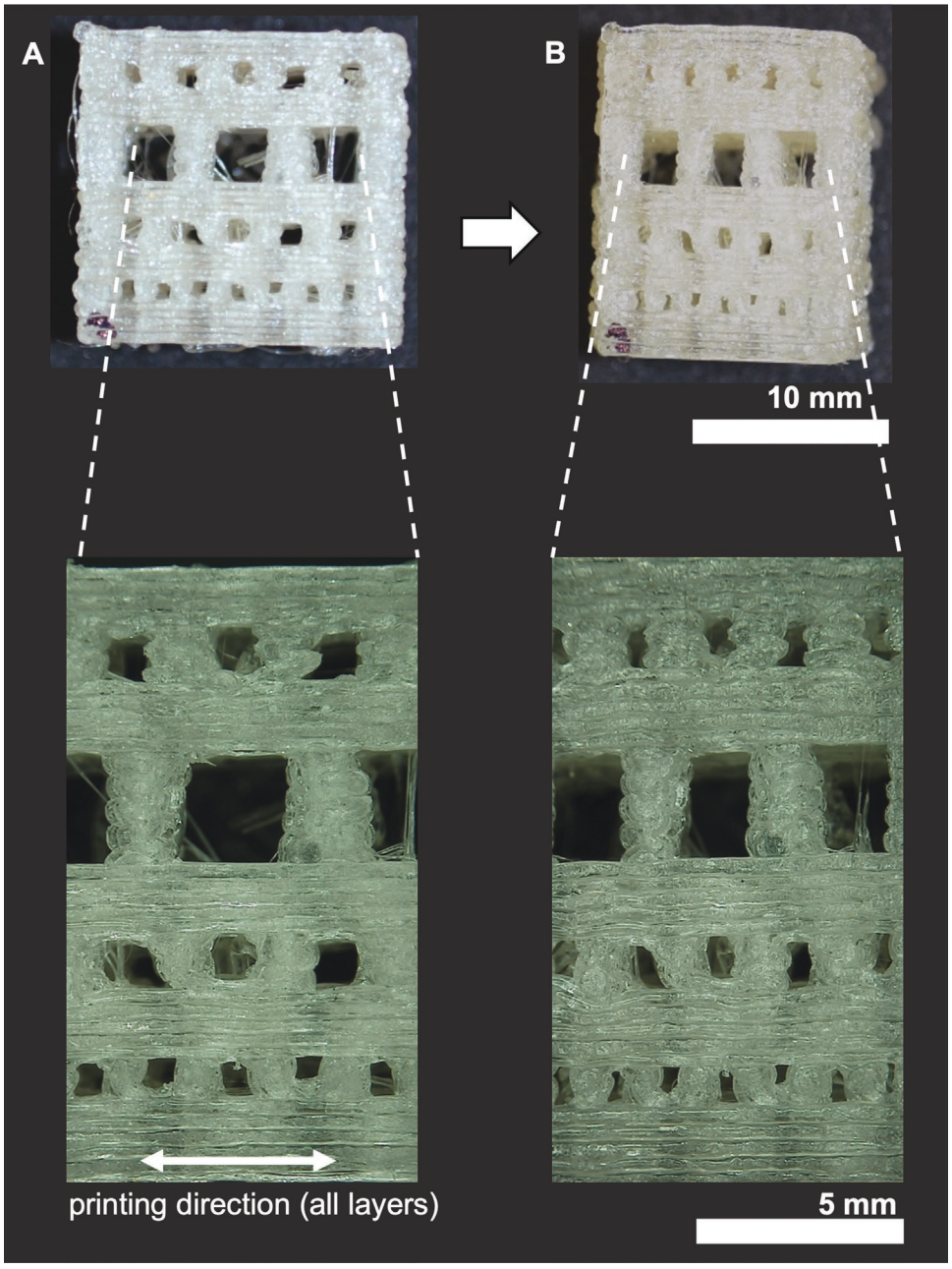

Figure 6. Representative images of 3D cubic samples with three different pore sizes A) before and B) after recovery. All pores contracted in the direction of the fibers.

had a similar total change in area (34.8%), however contraction was uniform in the x and y directions, and the magnitude of contraction of the pores increased substantially. While the printed fibers in the linear infill pattern connect opposite sides of the cube, the hexagonal fibers connect one side to both an opposite and adjacent side, and so as the fiber contracts two sides are pulled closer to a third, which may allow the fibers to contract more freely throughout the entire scaffold, which could explain both the more uniform contraction and larger pore contraction.

2.7. Modeling of Linear Infill Geometry

Finite element analysis was conducted to understand the active shape change of a cube with a porous lattice where fiber orientation alternated between 0° and 90° printed layers (relative to the x axis; Figure S4, Supporting Information). Upon triggering, there is contraction in the x and y directions and expansion in the z direction, consistent with the behavior of the linear infill geometry (Figure 7A). For this example, the residual strain is found to be 0.16 by fitting the experimental shape change.

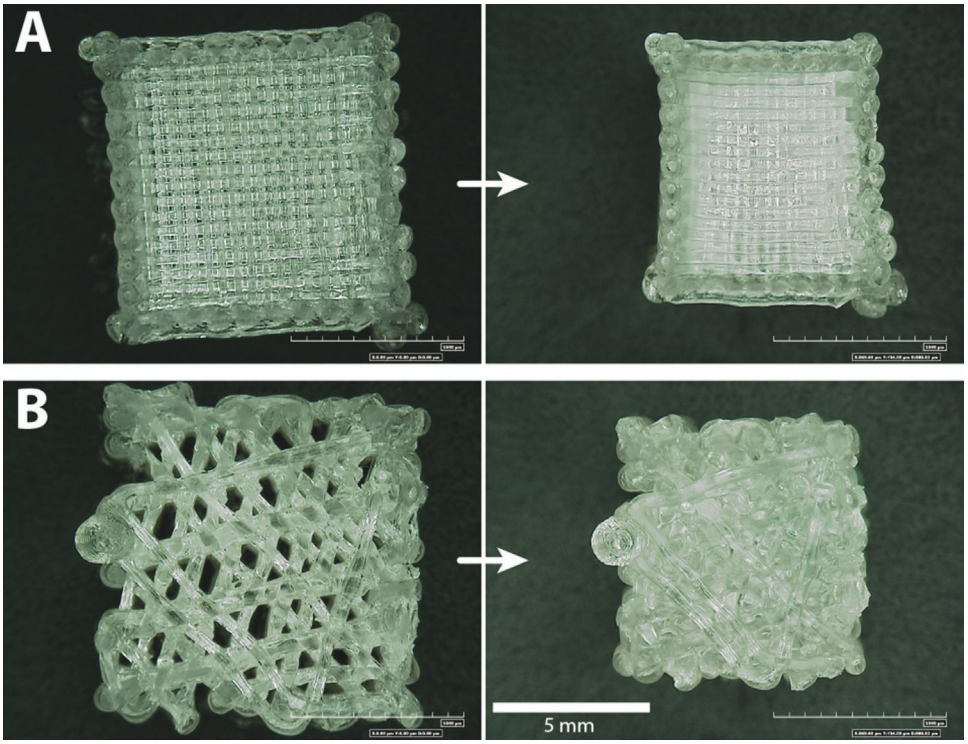

Figure 7. Representative image of cubes printed for cell scaffolding with A) alternating 0° and 90°, and B) hexagonal infill. The hexagonal infill led to a more uniform contraction upon recovery.

2.8. Proof-of-Concept Cell Culture Application

To provide demonstration of PvP in a model application, our specific goal was to address the challenge of obtaining an even cell distribution during cell seeding—a well-documented issue for 3D tissue culture and tissue engineering strategies.[31] 3D cell culture is often preferred to 2D culture in vitro because 3D culture can in many situations better recapitulate in vivo microenvironments and cell–cell interactions,[32–38] but in many applications the success of 3D culture is heavily dependent on obtaining a uniform, and often high density, cell distribution during seeding. Tissues grown from non-uniform and low cell densities are often inferior to their uniform/high cell density counterparts.[39] To address this challenge, many research groups have explored alternative seeding techniques, such as vacuum or spin seeding, to physically force cells more uniformly through the scaffold. However, drawbacks associated with these methods include cells being caught (effectively filtered) at the surface, which contributes to variable cell yields, and physical damage to the cells due to high shear stress, which can lead to a loss in viability.[40,41] Such effects have been previously studied by Solchaga et al.,[39] whose goal was to address technical issues, such as cell seeding homogeneity, with the goal of creating viable cartilage implants. In that work, passive seeding led to poor cell penetration, potentially due to cells plugging the pores.

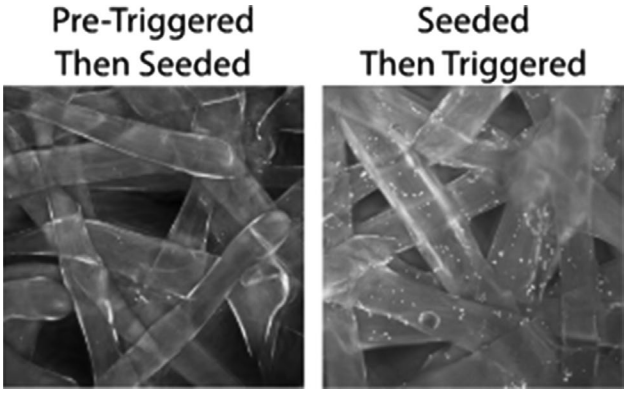

Figure 8. Representative fluorescence micrographs used to determine cell distribution in (left) pre-triggered and (right) active samples. Fiber diameter is ≈0.3 mm.

To address this challenge, we designed a porous, 3D biomedical scaffold that would self-contract after cell seeding. Thus, the scaffold, in its post-printed state, would contain large pores through which cells could precipitate during seeding and, after seeding, would contract to a smaller pore size more conducive to cell growth. Based on the infill geometry recovery characterization results, we printed $9 \times 9 \times 8$ mm scaffold at 210 °C with a multiplier of 1.0. Infill was set to 65% with a hexagonal pattern.

After recovery at 40 °C, scaffold pore area contracted by 32.3 ± 4.1% compared to the as-printed pore size (**Figure 8**). The number of cells in the top third and bottom third of the scaffolds was significant different between the active PvP scaffolds and the pre-triggered scaffolds ($p = 0.012$ and $p = 0.0006$, respectively, **Figure 9**), with the active PvP scaffolds having cells relatively evenly distributed throughout but the pre-triggered scaffolds having the largest number of cells in the top third of

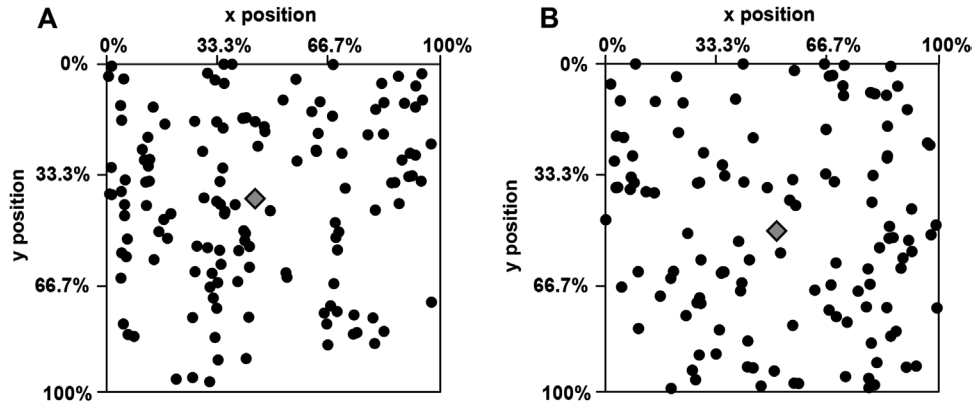

Figure 9. Illustration of x and y position of normalized cell distributions within cross section of representative A) pre-triggered and B) active PvP scaffolds. The diamond marker identifies the calculated centroid of the cells in that panel.

the scaffold, fewer in the middle, and the fewest at the bottom (Figures 9 and 10A). The distribution observed in the pre-triggered scaffolds is generally that observed with traditional static scaffolds with small pores: many cells become trapped near the top of the scaffold, which essentially acts as a filter. The pre-triggered samples contained 42 ± 2.0, 36 ± 3.0, and 22 ± 2.0 cells in the top, middle, and bottom thirds of the scaffold (per depth of field), respectively (Figures 9A and 10A). The total average cell count for the depth of field was 146 ± 10.0 cells (**Figure 10**B). The active PvP scaffolds contained 33 ± 3.6, 32 ± 4.0, and 35 ± 1.0 cells in the top, middle, and bottom thirds of the scaffold (per depth of field), respectively (Figures 9B and 10A). The total average cell count for the depth of field was 135 ± 18.0 cells (Figure 10B). No significant difference was found for the total number of cells in the pre-triggered vs. active PvP scaffolds.

Although a significant difference was observed in the cell distributions of the active PvP scaffolds and the pre-triggered scaffolds, it is important to note that in both scaffolds the pore dimensions (and the fiber diameters used to form those pores) were larger by one to two orders of magnitude than those present in many 3D biomedical scaffolds.[39] As a result, we would anticipate that scaffolds printed using smaller diameter FFF fibers and smaller resultant pores would result in greatly increased performance of the active PvP scaffold relative to the pre-triggered scaffold or similar benchmark static control scaffolds.

3. Conclusions

In conclusion, we have demonstrated the feasibility of trapping strain in individual fibers during extrusion-based fused filament fabrication, a process we refer to as programming via printing (PvP). We have shown that strain can be trapped not only in solid printed parts—such as layers or 3D objects with 100% infill—but also in fibers that span negative space in porous parts. The results further reveal different strain trapping behaviors in solid and porous printed parts. Recovery of solid parts is dominated by previously observed bending behaviors,[18,19] likely due to a non-uniform relaxation during printing that upon cooling causes a gradient of trapped strain. In contrast, recovery of porous parts primarily containing fibers spanning negative space shows uniform spatial recovery free from bending. We also found that that infill geometry can affect both the magnitude and spatial uniformity of trapped strain recovery. Lastly, in application to fabrication of cell scaffolds, we

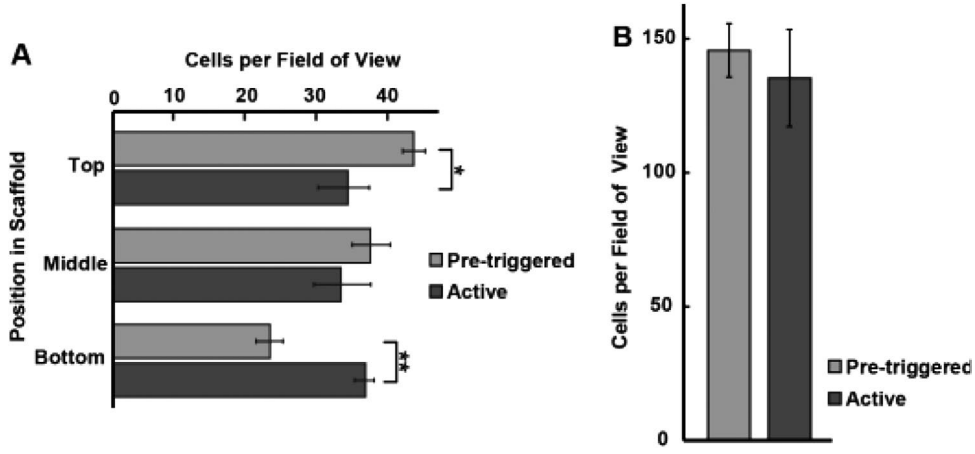

Figure 10. Quantification of A) the average number of cells present in the top, middle, and bottom thirds of scaffolds with B) corresponding total cell per field of view. (Sample size (n) = 3; Student's t-test; mean ± SD; *$p < 0.05$; **$p < 0.01$).

create a scaffold that can contract to trap cells in a distribution more uniform than that of a static scaffold and thereby illustrate the potential for PvP to provide new strategies to address unmet needs in biomedical and other fields.

4. Experimental Section

Shape-Memory Polymer and 3D Printing: All samples were prepared using a shape-memory thermoplastic polyurethane (SMP MM4520, SMP Technologies, Japan) filament with a dry T_g of 45 °C (and a wet T_g of 30 °C due to the plasticizing effect of hydration, confirmed by differential scanning calorimetry) 3D printed using a Makerbot Replicator 2×.

Single-Line Samples (1D): To trap strain into 1D fibers during printing, single lines (12 mm × 0.3 mm × 0.2 mm) were printed at a constant speed of 4200 mm min^{-1} using temperatures of 215 and 225 °C and an extrusion multiplier of 0.95 and 1.00. Five samples of each temperature and multiplier combination were printed. The build plate remained unheated for all experiments reported in this study.

Single-Layer Rectangular Samples (2D): Single-layer rectangular samples (28 mm × 8 mm × 0.2 mm) were printed at 4200 mm min^{-1} with the same temperatures and multipliers as the single line samples. Additionally, the fiber orientation of each sample was varied at 0°, 45°, or 90° relative to the long axis. Eight samples of each set of parameters were printed.

Recovery and Characterization of 1D and 2D Samples: For characterization of single-line samples, samples were imaged and measured using a Hirox Digital Microscope (Model KH-8700). The linear measurement tool was used to measure the length of the original geometry. Samples were then recovered in a water bath at 70 °C for 5 min. After recovery, the samples were re-measured. Programmed strain in each geometry was calculated using the following equation:

$$\varepsilon_L = \frac{L_0 - L_i}{L_0} \tag{1}$$

here L_0 and L_i are the fiber length before and after recovery, respectively.

For characterization of single-layer samples, five samples of each experimental group were recovered using a dynamic mechanical analyzer (DMA) to determine uniaxial strain. Samples were fastened to the tension clamp and the temperature was ramped to 70 °C at 5 °C min^{-1} and held isothermally for 5 min, then ramped down 5 C min^{-1} to 25 °C. Initial and recovered lengths were recorded and the strain was calculated using Equation (1). The remaining three samples in each group were recovered freely in the water bath at 70 °C to observe the final geometries.

Modeling Approach: From the experiments, contraction in the fiber direction ($\mathbf{n}_p$) was observed, with little change along its orthogonal direction ($\mathbf{m}_p$), and expansion in the normal direction $\mathbf{e}_z$ to the printing plane due to the Poisson effect. To develop a model fitting of the experimental data, an active deformation to a hyper-elastic model through a multiplicative decomposition of the total deformation gradient tensor $\mathbf{F}$ was introduced, such that

$$\mathbf{F} = \mathbf{F}^e\,\mathbf{F}^p \tag{2}$$

where $F_{ij} = \frac{\partial x_i}{\partial X_j}$, $i, j = 1,2,3$, and $\mathbf{X}$ and $\mathbf{x}$ are the configurations before and after deformation, respectively, $\mathbf{F}^p$ is the active part, and $\mathbf{F}^e$ is the elastic part of $\mathbf{F}$. According to the experimental observations, the active part $\mathbf{F}^p$ was chosen as

$$\mathbf{F}^p = \left(1-\varepsilon_p\right)\mathbf{n}_p \otimes \mathbf{n}_p + \mathbf{m}_p \otimes \mathbf{m}_p + \frac{1}{\left(1-\varepsilon_p\right)}\mathbf{e}_z \otimes \mathbf{e}_z \tag{3}$$

where $\mathbf{n}_p$ is the printing direction, $\mathbf{m}_p$ is the orthogonal direction of $\mathbf{n}_p$ on the printing plane, $\mathbf{e}_z$ is the normal direction of the printing plane, and ε_p is the residual strain. The residual strain ε_p is a fitting parameter, which can have a gradient along the thickness direction and is extracted by matching the contractions in experiments and simulations. Furthermore, the strain energy density was expressed in terms of the elastic component $\mathbf{F}^e$

$$U = \frac{1}{2}\mu\left(I_1^e - 3 - 2\ln J\right) + \frac{\lambda}{2}(\ln J)^2 \tag{4}$$

where μ is the shear modulus, λ is the Lame constant, $I_1^e = tr\left(F^{eT}F^e\right)$ is the first invariant of the right Cauchy–Green deformation tensor associated with $\mathbf{F}^e$ and $J = \det(\mathbf{F}) = \det(\mathbf{F}^e)$ by noticing $\det(\mathbf{F}^p) = 1$. The model has been shown to be able to capture the shape morphing induced by the residual strain in 3D printed thermoplastic polyurethanes and polylactic acid composites.[25] The shape changes were simulated using finite element analysis with implementation of the material model in the package FEniCS.[42]

Cubic Scaffolds (3D): 16 × 15 × 16 mm cubes possessing pores of three different cross-sectional dimensions (0.9, 6.5, and 0.48 mm^2) were printed. The fiber orientation was held constant in each layer, so that contraction would occur in only one direction. Based on the findings of the 1D and 2D studies and on prior work printing SMP MM4520,[43] all samples were printed at a temperature of 215 °C, multiplier of 1.0, and speed of 4200 mm min^{-1} on an unheated build-plate.

Recovery and Characterization of 3D Cubic Samples: The post-printing cube dimensions and pores were measured with the Hirox microscope, then recovered in a water bath at 70 °C for 10 min. The dimensions and pores were remeasured, and the change in area was calculated using the following equation:

$$\varepsilon_A = \frac{A_0 - A_i}{A_0} \tag{5}$$

where A_0 is the area before recovery and A_i is the area after recovery. The pores sizes of the hexagonally infilled scaffolds were measured using ImageJ.

Modeling of Cubic Scaffolds (3D): The simulated structure was discretized into second order tetrahedral elements. A mixed finite element scheme was employed to be able to describe the nearly incompressible material property of the SMP, where displacement and pressure are independent variables and interpolated with second and first order shape functions, respectively.

Linear and Hexagonal Infill Geometry: Based on the findings of the 1D and 2D studies and on prior work printing SMP MM4520,[43] all samples were printed at a temperature of 215 °C, multiplier of 1.0, and speed of 4200 mm min^{-1} on an unheated build-plate.

Recovery and Characterization of Linear and Hexagonal Infill Geometry: To quantify the trapped strain within the scaffolds, the as-printed sample fibers, dimensions, and pores of the linearly infilled samples were measured with a Hirox Digital Microscope (Model KH-8700). The same process was used for the hexagonally infilled sample, but with the measurement performed using ImageJ. Samples were then recovered in a water bath at 70 °C for 10 min, to allow for complete recovery, and reimaged and remeasured. Trapped strain in fibers was calculated using Equation (1). The overall scaffold change in area and the change in pore size area were both calculated using Equation (5).

Proof-of-Concept Cell Culture Application: Once printed, scaffolds were sterilized in ethanol for 1 h and dried for 24 h, then rinsed in sterile phosphate buffered saline (PBS) and conditioned with Basal Medium Eagle (BME) with 10% fetal bovine serum for 1 h to assist cell attachment. To achieve contraction, scaffolds in BME with 10% fetal bovine serum at 40 °C were chosen to recover, a physiologically relevant temperature that, if sufficiently brief, could be used in vivo or during cell culture while maintaining cell viability (**Figure 11**). For static seeding controls, scaffolds were triggered prior to cell seeding (pre-triggered).

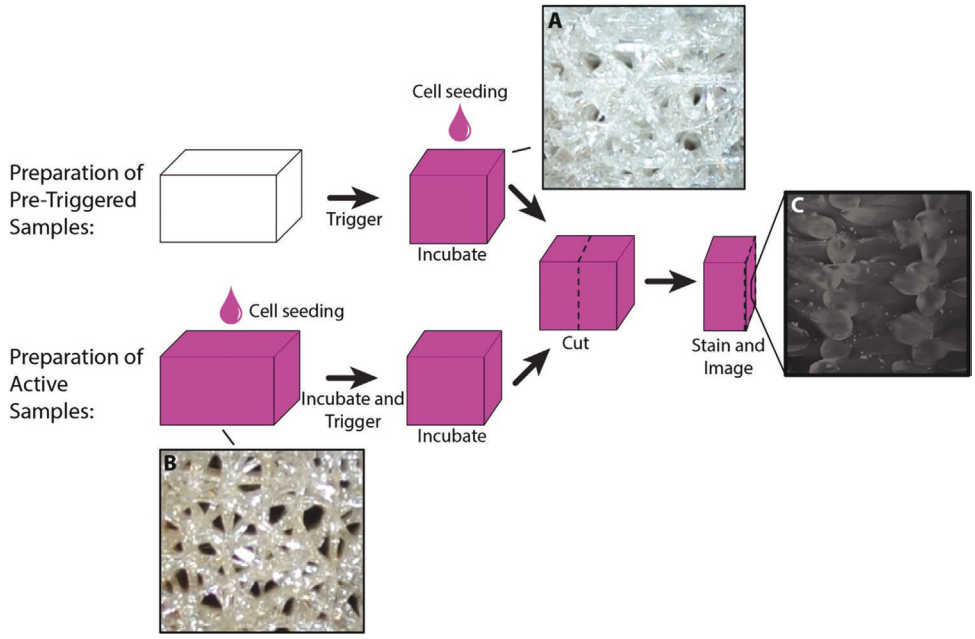

Figure 11. Design of cell culture experiments. Micrographs are shown to illustrate pore condition upon cell seeding for A) pre-triggered, B) active scaffold, and C) imaging of cell distribution in a sliced scaffold after culture.

C3H10T1/2 murine fibroblasts (ATCC) were chosen due to the prior extensive experience with their use in characterizing SMP substrates and scaffolds[5,44] and were cultured as previously described.[5] Cells were collected and used for experiments at passage number fifteen, and scaffolds were solution seeded in 24-well plates at 30 000 cells cm^{-3} and incubated at 30 °C. After 2 h, the active PvP scaffolds were transferred to a 40 °C incubator for 22 h to fully recover. The pre-triggered scaffolds remained in the 30 °C incubator for the entire 24 h. Afterward, cells were fixed to their scaffolds using 4% paraformaldehyde. Next, three scaffolds from each group were cut with a razor blade from top to bottom through the center. Cells were treated with triton solution to permeate the cells, and DAPI stain (Invitrogen) was applied following the manufacturer's instructions.

To quantify cell distribution, cells were imaged at 10× with a Leica DMI 4000B inverted fluorescent microscope with a Leica DFC 340FX camera using the multi acquisition option in μManager.[45] The X-Y position was manually set to image the entire scaffold cross section, and Z-stacks of images were taken at each position with nine 100 µm increments for a total depth of field of 0.9 mm through the 5× lens. To create a single image with the entire depth of field, each Z-stack was processed with the "Extended Depth of Field" plugin in ImageJ.[46] To isolate the cells in the image, the threshold was manually adjusted processed with the "Watershed" function.[47] To both count and record the positions of the cells, the adjusted image was processed with the "Analyze Particles" function.[47] The labeled Y positions of the cells were normalized with respect to the length of the scaffold, and the numbers of cells in the top, middle, and bottom third were quantified.

Statistical Analysis: Summary statistics present mean ± SD. Sample size (n) for each statistical analysis is identified in the associated results or experimental subsection above. Data from the single line (1D) and single layer (2D) samples were evaluated using 2-way ANOVA, followed by Tukey post-hoc. Bars show sample SD. Student's t-test was used to determine if the difference in cell number was significant in each third of the scaffold and if the total number of cells was significantly different. Results were considered significant at $p < 0.05$. All comparisons were made using the R statistical analysis software (R Core Team, 2019).

Supporting Information

Supporting Information is available from the Wiley Online Library or from the author.

Acknowledgements

The authors gratefully acknowledge Hongyu Fan for his modeling and simulation contributions, Paul Chando for his expertise in 3D printing fabrication, and Zhuoqi (Chi Chi) Tong for his assistance with CAD and printing preparation. Financial support for this project was provided by the National Science Foundation Biomaterials and Advanced Manufacturing programs (DMR-1609523 and CMMI- 2022421), the National Institutes of Health National Institute of General Medical Sciences (R21 GM141573-01), the Syracuse University Collaboration of Unprecedented Success and Excellence (CUSE) program, and the Syracuse University Research Excellence Doctoral Funding program.

Conflict of Interest

The authors declare no conflict of interest.

Data Availability Statement

The data that support the findings of this study are available from the corresponding author upon reasonable request.

Keywords

active scaffolds, 3D cell cultures, shape-memory polymers, self-shrinking, SMP MM-4520

Received: November 23, 2022
Revised: January 9, 2023
Published online: February 7, 2023

[1] P. T. Mather, X. F. Luo, I. A. Rousseau, *Annu. Rev. Mater. Res.* **2009**, *39*, 445.
[2] M. E. Pede, J. H. Henderson, in *Polymer and Photonic Materials towards Biomedical Breakthroughs*, Results and Discussion Springer, Cham, **2018**.
[3] I. A. Rousseau, *Polym. Eng. Sci.* **2008**, *48*, 2075.
[4] R. M. Baker, L. F. Tseng, M. T. Iannolo, M. E. Oest, J. H. Henderson, *Biomaterials* **2016**, *76*, 388.
[5] K. A. Davis, K. A. Burke, P. T. Mather, J. H. Henderson, *Biomaterials* **2011**, *32*, 2285.
[6] K. A. Davis, X. F. Luo, P. T. Mather, J. H. Henderson, *JoVE-J. Visualized Exp.* **2011**, *53*, e2903.
[7] A. Lendlein, R. S. Langer, (Helmholtz Zentrum Geesthacht Zentrum fuer Material und Kustenforschung GmbH), U.S. Patent 8,834,522, **2014**.
[8] M. B. B. Monroe, A. D. Easley, K. Grant, G. K. Fletcher, C. Boyer, D. J. Maitland, *ChemPhysChem* **2018**, *19*, 1999.
[9] G. Passucci, M. E. Brasch, J. H. Henderson, V. Zaburdaev, M. L. Manning, *PLoS Comput. Biol.* **2019**, *15*, e1006732.
[10] L.-F. Tseng, P. T. Mather, J. H. Henderson, *Acta Biomater.* **2013**, *9*, 8790.
[11] L. F. Tseng, J. Wang, R. M. Baker, G. R. Wang, P. T. Mather, J. H. Henderson, *Tissue Eng., Part A* **2016**, *22*, 1026.
[12] J. Wang, M. E. Brasch, R. M. Baker, L. F. Tseng, A. N. Pena, J. H. Henderson, *J. Mater. Sci.: Mater. Med.* **2017**, *28*, 151.
[13] Q. Ge, A. H. Sakhaei, H. Lee, C. K. Dunn, N. X. Fang, M. L. Dunn, *Sci Rep* **2016**, *6*, 31110.
[14] F. Momeni, S. M. N. Mehdi Hassani, X. Liu, J. Ni, *Mater. Des.* **2017**, *122*, 42.
[15] J. E. M. Teoh, J. An, C. K. Chua, M. Lv, V. Krishnasamy, Y. Liu, *Virtual Model. Rapid Manuf.: Adv. Res. Virtual Rapid Prototyping, Proc. Int. Conf. Adv. Res. Rapid Prototyping, 2nd*, **2017**, Vol. *12*, p. 61.
[16] D. Zhang, O. J. George, K. M. Petersen, A. C. Jimenez-Vergara, M. S. Hahn, M. A. Grunlan, *Acta Biomater.* **2014**, *10*, 4597.
[17] W. Abuzaid, M. Alkhader, M. Omari, *Polym. Test.* **2018**, *68*, 100.
[18] M. Bodaghi, A. R. Damanpack, W. H. Liao, *Mater. Des.* **2017**, *135*, 26.
[19] G. F. Hu, A. R. Damanpack, M. Bodaghi, W. H. Liao, *Smart Mater. Struct.* **2017**, *26*, 125023.
[20] A. Lendlein, M. Behl, B. Hiebl, C. Wischke, *Expert Rev. Med. Devices* **2010**, *7*, 357.
[21] A. Lendlein, R. Langer, *Science* **2002**, *296*, 1673.
[22] R. Noroozi, M. Bodaghi, H. Jafari, A. Zolfagharian, M. Fotouhi, *Polymers* **2020**, *12*, 519.
[23] J. Wang, A. Quach, M. E. Brasch, C. E. Turner, J. H. Henderson, *Biomaterials* **2017**, *140*, 150.
[24] I. Akbar, M. El Hadrouz, M. El Mansori, D. Lagoudas, *J. Manuf. Processes* **2022**, *76*, 335.
[25] B. An, Y. Tao, J. Gu, T. Cheng, X. A. Chen, X. Zhang, W. Zhao, Y. Do, S. Takahashi, H.-Y. Wu, presented at *Proceedings of the 2018 CHI Conference on Human Factors in Computing Systems*, Montréal, Canada **2018**, pp. 1-12.
[26] L. Kačergis, R. Mitkus, M. Sinapius, *Smart Mater. Struct.* **2019**, *28*, 105042.
[27] T. van Manen, S. Janbaz, A. A. Zadpoor, *Mater. Horiz.* **2017**, *4*, 1064.
[28] M. Bodaghi, R. Noroozi, A. Zolfagharian, M. Fotouhi, S. Norouzi, *Materials* **2019**, *12*, 1353.
[29] Y. Mao, K. Yu, M. S. Isakov, J. Wu, M. L. Dunn, H. J. Qi, *Sci. Rep.* **2015**, *5*, 13616.
[30] Q. Y. Guo, P. T. Knight, P. T. Mather, *J. Controlled Release* **2009**, *137*, 224.
[31] G. Vunjak-Novakovic, B. Obradovic, I. Martin, P. M. Bursac, R. Langer, L. E. Freed, *Biotechnol. Prog.* **1998**, *14*, 193.
[32] M. J. Bissell, A. Rizki, I. S. Mian, *Curr. Opin. Cell Biol.* **2003**, *15*, 753.
[33] D. Cawkill, S. S. Eaglestone, *Drug Discovery Today* **2007**, *12*, 820.
[34] A. J. Engler, S. Sen, H. L. Sweeney, D. E. Discher, *Cell* **2006**, *126*, 677.
[35] P. M. Gilbert, K. L. Havenstrite, K. E. G. Magnusson, A. Sacco, N. A. Leonardi, P. Kraft, N. K. Nguyen, S. Thrun, M. P. Lutolf, H. M. Blau, *Science* **2010**, *329*, 1078.
[36] L. G. Griffith, M. A. Swartz, *Nat. Rev. Mol. Cell Biol.* **2006**, *7*, 211.
[37] M. Kapałczyńska, T. Kolenda, W. Przybyła, M. Zajączkowska, A. Teresiak, V. Filas, M. Ibbs, R. Bliźniak, Ł. Łuczewski, K. Lamperska, *Arch. Med. Sci.* **2018**, *14*, 910.
[38] J. Lee, M. J. Cuddihy, N. A. Kotov, *Tissue Eng., Part B* **2008**, *14*, 61.
[39] L. A. Solchaga, E. Tognana, K. Penick, H. Baskaran, V. M. Goldberg, A. I. Caplan, J. F. Welter, *Tissue Eng.* **2006**, *12*, 1851.
[40] J. C. Merchuk, *Adv. Biochem. Eng./Biotechnol.* **1991**, *44*, 65.
[41] M. Pei, L. A. Solchaga, J. Seidel, L. Zeng, G. Vunjak-Novakovic, A. I. Caplan, L. E. Freed, *FASEB J.* **2002**, *16*, 1691.
[42] M. Alnæs, J. Blechta, J. Hake, A. Johansson, B. Kehlet, A. Logg, C. Richardson, J. Ring, M. E. Rognes, G. N. Wells, *Arch. Numer. Software* **2015**, *3*, 100.
[43] K. Pieri, B. M. Felix, T. Zhang, P. Soman, J. H. Henderson, *3D Print. Addit. Manuf, ahead of print* **2021**, https://doi.org/10.1089/3dp.2021.0072.
[44] S. L. Buffington, J. E. Paul, M. M. Ali, M. M. Macios, P. T. Mather, J. H. Henderson, *Acta Biomater.* **2019**, *84*, 88.
[45] A. D. Edelstein, M. A. Tsuchida, N. Amodaj, H. Pinkard, R. D. Vale, N. Stuurman, *J. Microbiol. Methods* **2014**, *1*, e10.
[46] B. Forster, D. Van de Ville, J. Berent, D. Sage, M. Unser, *Microsc. Res. Tech.* **2004**, *65*, 33.
[47] J. Schindelin, I. Arganda-Carreras, E. Frise, V. Kaynig, M. Longair, T. Pietzsch, S. Preibisch, C. Rueden, S. Saalfeld, B. Schmid, J.-Y. Tinevez, D. J. White, V. Hartenstein, K. Eliceiri, P. Tomancak, A. Cardona, *Nat. Methods* **2012**, *9*, 676.